



Active movement of the Cascade landslide complex in Washington from a coherence-based InSAR time series method



Xiaopeng Tong ^{*,1}, David Schmidt

Department of Earth and Space Sciences, University of Washington, Seattle, WA, United States

ARTICLE INFO

Article history:

Received 8 February 2016
Received in revised form 16 August 2016
Accepted 12 September 2016
Available online 16 September 2016

Keywords:

Landslide hazards
Cascade landslide complex
InSAR time-series

ABSTRACT

We used interferometric synthetic aperture radar (InSAR) data from the ALOS-1 satellite to investigate the active movement of landslides along the Columbia River Gorge from 2007–2011. To increase the spatial extent of the deformation signal, we developed a coherence-based small-baseline subset (SBAS) method and derived the time series of the landslide movement. We find no significant movement on the previously mapped Washougal, Sakamania, Oregon Shore, and Wind Mountain landslides. However, we document the slow movement of the Redbluff landslide, which is part of the Cascade Landslide Complex. The InSAR data reveal up to approximately 25 cm of line-of-sight displacement over the 4-year observation period. The Redbluff landslide is seasonally activated, with accelerated movement observed during the early winter of each year. The amplitude of the seasonal signal is variable from year-to-year, with the greatest movement observed in early winter of 2009 and 2011. To assess the triggering mechanisms, we compared the displacement time series data with local precipitation data. The deformation correlated well with precipitation, implying the slow movement is controlled by rainfall that infiltrates to the base of the slide.

© 2016 Elsevier Inc. All rights reserved.

1. Introduction

Advances in Interferometric Synthetic Aperture Radar (InSAR) observations have enabled researchers to measure deformation of the earth's surface over time with high spatial resolution (10's of meters) and line-of-sight precision (~millimeters). The satellite-based observations have proven to be a useful tool for studying and monitoring landslide activity (Colesanti and Wasowski, 2006; Wasowski and Bovenga, 2014). For example InSAR has shown that the velocity of the slow-moving landslide oscillates seasonally in response to seasonal variations of precipitation (Hilley et al., 2004; Handwerger et al., 2013). InSAR data is also useful for mapping the perimeter of active movement, which aids in the assessment of landslide hazards (Calabro et al., 2010; Zhao et al., 2012; Scheingross et al., 2013; Milillo et al., 2014).

The Cascade Landslide Complex (CLC) is a prominent morphological feature within the Columbia River Gorge, and the slide has been well documented in the stories of Native Americans and western explorers (Fig. 1). The CLC is comprised primarily of four distinct lobes. From west to east, they are the Carpenters Lake, the Bonneville, the Redbluff, and the Moseley Lake landslides. Of these landslide lobes, the most recent catastrophic movement occurred at the Bonneville landslide between 1425 and 1450 CE, as dated by tree samples (O'Connor and

Burns, 2009). This landslide deposit was large enough to dam the Columbia River, and the resulting natural dam was dubbed as the "Bridge of the Gods" in the local tribal folklore. The Columbia River eventually eroded the dam, the remnants of which created a series of cascades (O'Connor et al., 1996). The Lewis and Clark expedition encountered these cascades in 1805 on their quest to reach the Pacific Ocean. Given that the cascades were too energetic for safe passage, the expedition party was forced to portage around the rough stretch of river for several kilometers. It is from this particular section of the Columbia River, which is now submerged behind the modern Bonneville dam, that the Cascade mountain range derives its name.

The CLC is located along the northern riverbank of the Columbia River, near Stevenson, Washington, one of several large landslide complexes found along the bluffs (Palmer, 1977). The CLC represents the deep-seated failure of Table Mountain and Greenleaf Peak, which rise ~1 km above the Columbia River. The geology of the CLC is composed of Miocene-age Columbia River Basalt overlying the weakly lithified volcanoclastic rocks of the Eagle Creek Formation. Below the Eagle Creek formation is the older Ohanapeosh Formation, composed of volcanic and pyroclastic debris deposits (Wise, 1970; Palmer, 1977). On top of the Columbia River Basalt group are the calc-alkaline lavas and volcanoclastic detritus associated with modern volcanic activity (O'Connor and Burns, 2009). The CLC is monitored by the U.S. Geological Survey because of its geological history and hazard potential. Randall (2012) mapped the boundaries of the main active lobe of the slide, and he identified collapse events and rock avalanches on the Redbluff landslide. While field mapping and digital terrain maps help to

* Corresponding author.

E-mail addresses: xitong@uw.edu (X. Tong), dasc@uw.edu (D. Schmidt).

¹ Mailing address: Johnson Hall Rm-070, Box 351310, 4000 15th Avenue NE, Seattle, WA 98195-1310, U.S.A.

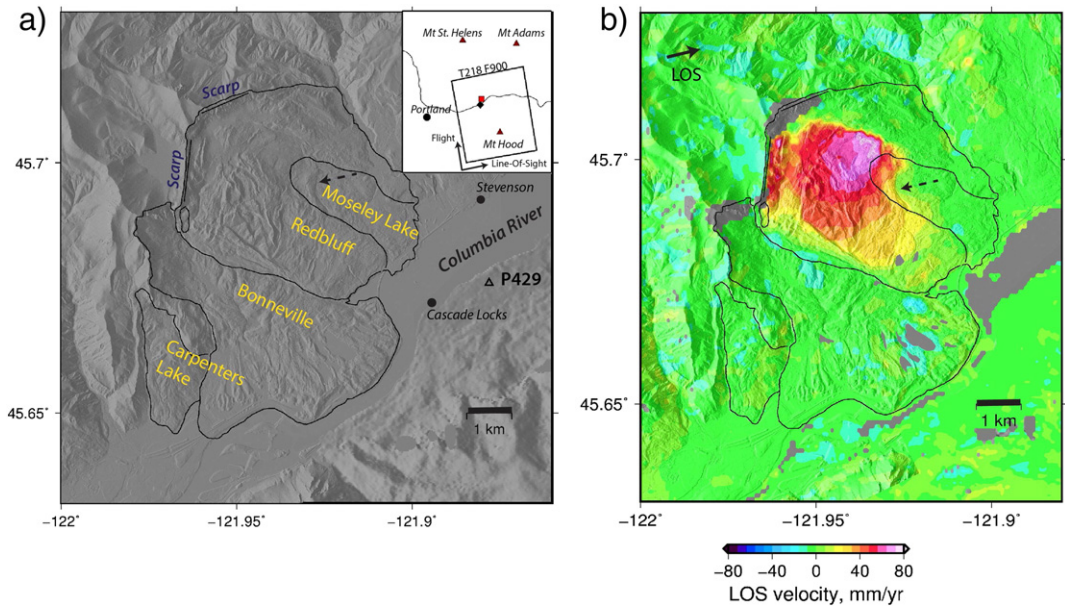


Fig. 1. a) Shaded relief map of the Cascade Landslide Complex and the Columbia River Gorge from LiDAR DEM. The four main lobes of the landslide complex (Carpenters Lake, Bonneville, Redbluff and Moseley Lake landslides) are outlined with black lines (Randall, 2012). A continuous GPS site is marked by the open triangle. The inset map to the upper right shows the location of the Cascade Landslide Complex (red square) relative to Portland, Oregon. The footprint of the ascending ALOS-1 radar imagery (track 218, frame 900) is shown by the black box. The other symbols indicate the major cities and towns (black filled circles), the major volcanoes (red triangles), and the meteorological site that provided the daily precipitation value used in this study (black diamond). b) Average line-of-sight velocity (a best-fit estimate to displacement time series) measured by InSAR of the Cascade Landslide Complex. Warm colors indicate motion away from the satellite in the look direction (black solid arrow). The background shading is based on the 2 m-resolution DEM from LiDAR. The black dashed arrow points to a discrepancy between the previous outline of the Moseley lake landslide and the boundary of active movement observed by InSAR (see text for details).

characterize the CLC, the extensive size and thick vegetated cover make it difficult to fully monitor active movement.

Here we investigate the movement of the slow-moving Cascade Landslide Complex with satellite-based InSAR data. Pierson and Lu (2009) used two-pass interferometry to first detect slow movement of the Redbluff landslide, and they confirmed this finding through field

reconnaissance. In this paper, we resolve the temporal and spatial evolution of movement on the CLC by solving for InSAR time series. We modify existing InSAR time-series algorithms to formally include radar decorrelation in the analysis, which helps to better resolve the displacement field and its temporal variability. Finally, we address whether the movement of the slow-moving landslide is correlated with precipitation

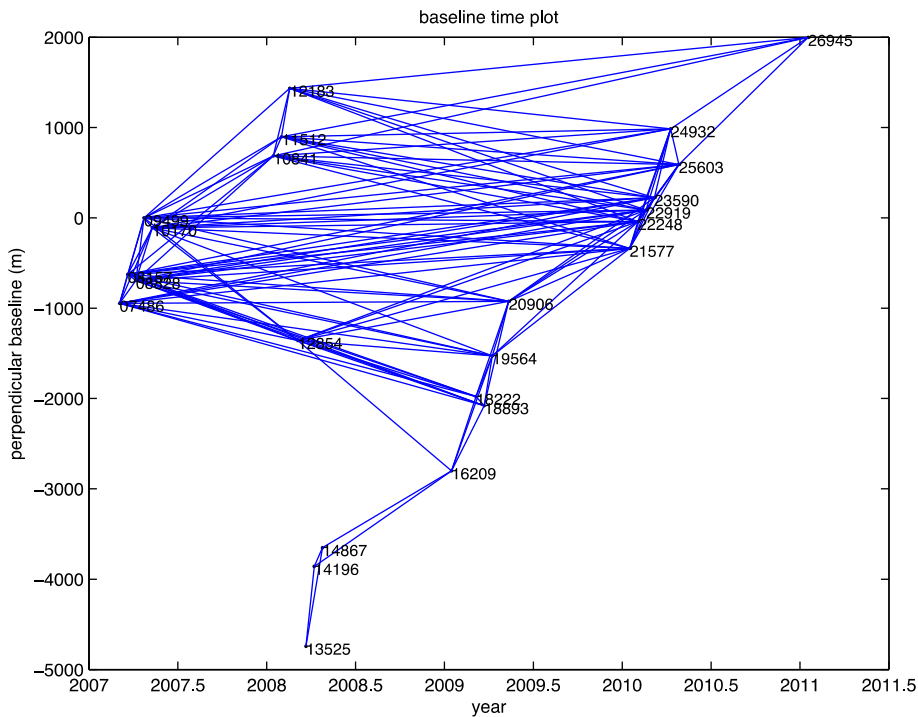


Fig. 2. Baseline-time plot of the ALOS-1/PALSAR-1 data from ascending track 218 frame 900. The blue lines indicate the set of SAR pairs used to form interferograms. Each 5-digit index is the orbital number of each SAR acquisition.

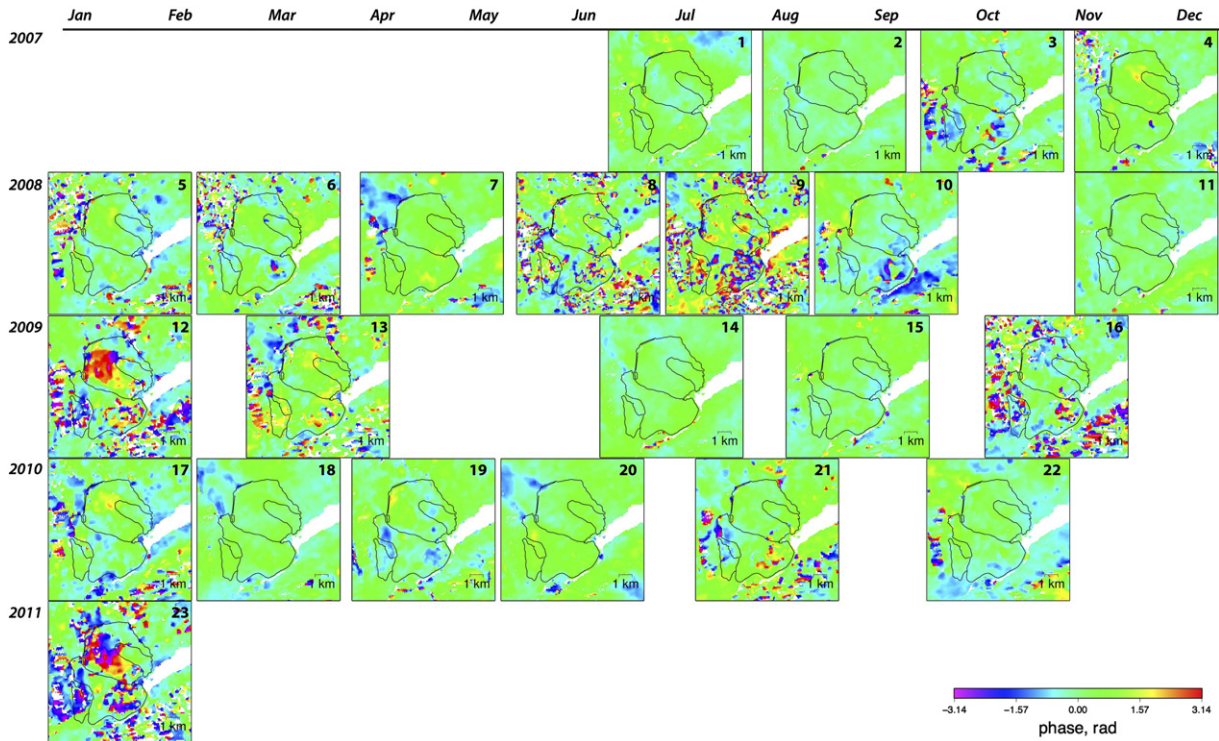


Fig. 3. An interferogram calendar of the landslide movement. Each frame corresponds to one 46-day or 92-day interferogram. The mapped landslide perimeter is marked by the thin black lines. Accelerated movement is detected by individual interferograms in early 2009 and 2011. The colored-speckled regions indicate noise in the wrapped interferograms.

rate. This study further demonstrates the utility of the satellite-based InSAR system for evaluating landslide hazards.

2. Data

We analyzed synthetic aperture radar (SAR) data from the Advanced Land Observing Satellite (ALOS-1) from 2007–2011. The footprint of the ALOS-1 satellite is shown in the inset map of Fig. 1a. The satellite flies along the ascending pass with the antenna looking down to the right. The incidence angle of the frame is approximately 38°. The PALSAR-1 instrument onboard the satellite operates with an L-band antenna (24 cm). Compared to other radar frequency bands, an L-band system typically performs better in highly vegetated environments, and the phase signal is less susceptible to temporal decorrelation (i.e. degradation of signal quality due to temporal change in backscattering).

The study area is imaged by 24 ALOS-1/PALSAR-1 scenes, from which we generated 133 interferograms using the open-source InSAR processing software GMTSAR (Sandwell et al., 2011) and the batch processing method (Tong et al., 2013). We use the SRTM30 digital elevation model to remove the topographic contribution to the interferometric phase (Farr and Kobrick, 2000). To reduce speckle noise, the interferograms are filtered and downsampled 4 pixels in range and 8 pixels in azimuth, in radar coordinates. After low-pass filtering and geocoding, the spatial resolution of a pixel is further reduced to approximately 200 m. The baseline of these interferograms is usually smaller than 1500 m. The baseline-time information of the SAR data is shown in Fig. 2. First, we analyzed the interferograms with the shortest temporal baseline to form a chain of differential interferograms. Most of these interferograms have a temporal resolution of 46 days. These consecutive interferograms maintain relatively good temporal sampling thanks to the fact that the SAR data are acquired relatively frequently over this region. Since there are 24 scenes in total, we obtained 23 consecutive interferograms spanning from 2007 to 2011. For two time periods, the interferograms had perpendicular baselines between 3000–4000 m, which is too close to the critical baseline to form an interferogram. We managed

to obtain phase information for these two periods indirectly by adding two interferograms sharing common scenes, although the results contain much more noise than the ones formed directly (Fig. 3).

We used the daily position time-series data product of a continuous GPS site (P429) of the Plate Boundary Observatory (PBO) to validate the InSAR data. The GPS site is located on the southern bank of the Columbia River where little landslide motion is expected. The location of this GPS site is marked as an open triangle in Fig. 1. We consider the positional time-series data from 2007–2011, which spans the same time period as the InSAR data. Along with the deformation data, we also analyzed the daily precipitation data from a nearby meteorological site (Bonneville Dam, Oregon, 3 km southwest of the CLC) to investigate the causality relationship between the landslide deformation and rainfall. The location of the Bonneville Dam meteorological site is marked as a black diamond in the inset map of Fig. 1.

3. InSAR time-series method

The InSAR Small-Baseline Subset (SBAS) method has been effective at retrieving temporal variations of the line-of-sight signal (Berardino et al., 2002; Schmidt and Bürgmann, 2003; Lanari et al., 2004; Lauknes et al., 2011; Fattahi and Amelung, 2013). It is less effective in highly

Table 1
Definition for Eqs. (1) and (2).

Symbol	Meaning
m_j	Incremental displacement for each epoch
d_i	LOS phase of the i th interferogram
B_i	Perpendicular baseline of the i th interferogram
β	Scale factor determined by radar wavelength and the incidence angle of the radar wave and the distance from the radar to the ground
W	Diagonal matrix containing coherence weights
γ_i	Coherence of the i th interferogram
Δh	DEM error
λ	Smoothing factor

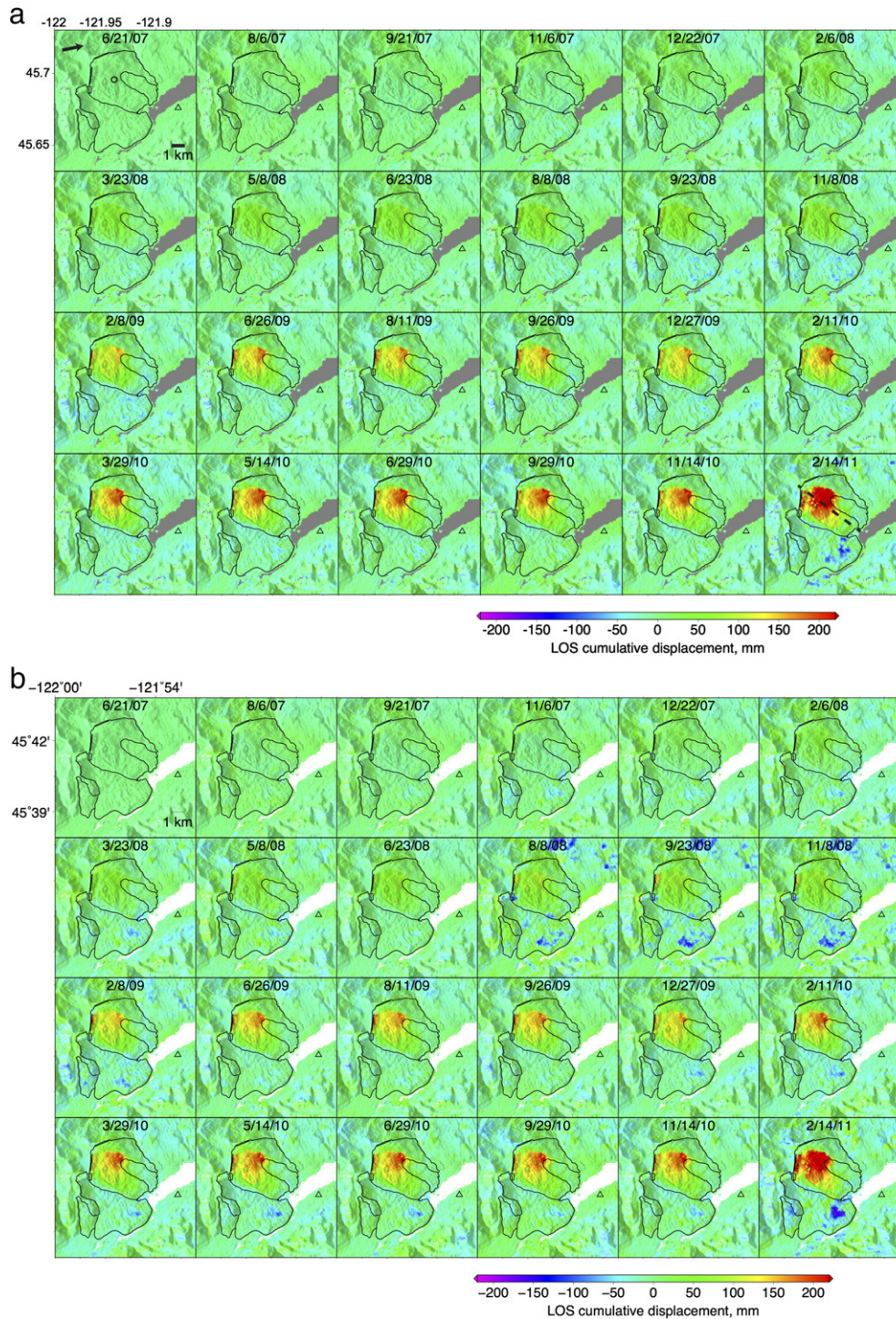


Fig. 4. a. Time-dependent displacement of the Cascade Landslide Complex from the InSAR time-series analysis that spans 2007–2011. The color scale indicates the cumulative displacement in the radar line-of-sight (LOS) direction, as indicated by the black arrow in the first frame. Positive LOS movement (red) corresponds to movement away from the satellite, which is consistent with downslope movement. The black lines show the outlines of the mapped landslides. The black triangle indicates the location of the continuous GPS site P429. The open black circle marks the location of the displacement time-series shown in Fig. 6. The black dash line in the last frame marks the location of the displacement profile shown in Fig. 9. The date (month/day/year) of each snapshot is marked at the top of each sub-image. b. The InSAR time-series result of the Cascade Landslide Complex from the non-weighted SBAS analysis to show the improvement with coherence weighting. If a mask is applied prior to unwrapping, then a significant fraction of the pixels would be removed from the final result.

vegetated environments because of decorrelation; pixels with high decorrelation (low coherence) are typically excluded from the analysis, thereby leading to diminished spatial coverage in the final InSAR map. A more careful treatment of decorrelation can be performed where the phase coherence, or other metric of signal quality, is used to weight the phase observations (Agram and Simons, 2015). The coherence is

typically determined by examining the phase variance of pixels within a spatial window (Rosen et al., 2000). Low coherence corresponds to an increase in the noise level of the InSAR phase measurements, and InSAR processing systems commonly use a coherence threshold to mask out noisy pixels. The interferograms are unwrapped by the SNAPHU software (Chen and Zebker, 2000) (SNAPHU stands for

Statistical-Cost, Network-Flow Algorithm for Phase Unwrapping). While unwrapping the interferograms, we have intentionally chosen not to mask the noisy phase with a coherence mask in order to use all available phase information. Unwrapping all the pixels, even the decorrelated ones, has the potential to introduce additional phase unwrapping error. However, the signal in the decorrelated pixels will be down-weighted in the time-series analysis.

We have improved the conventional SBAS methodology by introducing phase coherence of the interferograms into the inverse problem. Instead of discarding the noisy data present in a fraction of the interferograms, we keep all the pixels in the processing chain and weight the observed phase data based on the coherence for each pixel in each differential interferogram using the weighting matrix W . The coherence is estimated by taking the amplitude of the complex correlation function for each full resolution differential interferogram, averaged over an ensemble of phase pixels (window size of 4 in range and 8 in azimuth, in this case). Alternative algorithms for assessing signal quality could be used for this purpose, such as the phase variance (i.e. Rosen et al., 2000) or even the amplitude dispersion index (Ferretti et al., 2001). This coherence-based SBAS technique is less sensitive to the noise in the input data, and it results in a spatially coherent signal with dense coverage. The weighted least-squares inversion that operates on each phase pixel is:

$$W \begin{bmatrix} 1 & 1 & 0 & \dots & \beta B_1 \\ 0 & 1 & 1 & \dots & \beta B_1 \\ \dots & \dots & \dots & \dots & \dots \\ \lambda/\Delta t_1 & -\lambda/\Delta t_1 & 0 & \dots & 0 \\ 0 & \lambda/\Delta t_2 & -\lambda/\Delta t_2 & \dots & 0 \end{bmatrix} \begin{bmatrix} m_1 \\ m_2 \\ \dots \\ m_s \\ \Delta h \end{bmatrix} = W \begin{bmatrix} d_1 \\ d_2 \\ \dots \\ 0 \\ 0 \end{bmatrix} \quad (1)$$

$$W = \text{diag}\{\gamma_1, \gamma_2, \gamma_3, \dots, \gamma_n\} \quad (2)$$

The data kernel matrix has size of $[n \times s + 1]$, where n is the number of interferograms (133 in this case) and s is the number of temporal increments (23 in this case). When selecting interferograms in the SBAS analysis, we used more liberal criteria: the temporal baseline is smaller than 9000 days and the spatial baseline is smaller than 1500 m. All variables are defined in Table 1. We note that an iterative weighted least squares method or minimization based on L-1 norm could also be used to solve Eq. 1.

We solved the inverse problem (Eq. 1) on a pixel-by-pixel basis to obtain the final InSAR time-series of the cumulative line-of-sight displacement $M(t)$, such that $M(t) = \sum_{i=1}^t m_i$. We used the smoothing factor to penalize unrealistically large temporal fluctuations in the InSAR time-series. The choice of the temporal smoothing will affect the final displacement time-series. A common issue in the InSAR observations is that the temporal sampling is not regular. To give each epoch in the time-series an equal weight on temporal smoothing, we implemented a first-order differential smoothing factor λ that is scaled by the corresponding temporal interval of InSAR observations. The deformation on the landslide is usually not temporally steady, so it is expected to see accelerations of landslide movement. Since we don't have a priori information on how the landslide behaved, we experimented with a range of smoothing factors and examined the outcomes. The preferred value of the smoothing factor is validated by comparison with temporal fluctuation of independent data, including the GPS data at site P429 and precipitation data. Because the dimension of the landslide is less than 10 km, a Gaussian 20 km high-pass filter is applied to each unwrapped differential interferogram to enhance the localized landslide motion.

4. Results

The results of the improved SBAS algorithm help to better illuminate the kinematics the CLC, and they reveal a complex spatial and temporal pattern of the landslide movements (Fig. 4). Movement occurred initially at two places within the Redbluff landslide: the northwestern headscarp and a circular morphological feature in the main body of the slide. Before 2009, the cumulative displacement is relatively gradual and low amplitude. There is no significant deformation signal in the summer and fall seasons, and the landslide is mostly active during the winter and spring seasons.

4.1. Spatial pattern of movement

Deformation on the CLC is concentrated on the Redbluff landslide, with the average line-of-sight velocity reaching 40–80 mm/yr during the time period from 2007–2011 (Fig. 1b). No significant signal is detected on the other three landslide lobes. Fig. 5 shows a 3D perspective of the area of interests to emphasize the relationship of the active sliding and the hill slope. Important localities like the Cascade Locks, Stevenson,

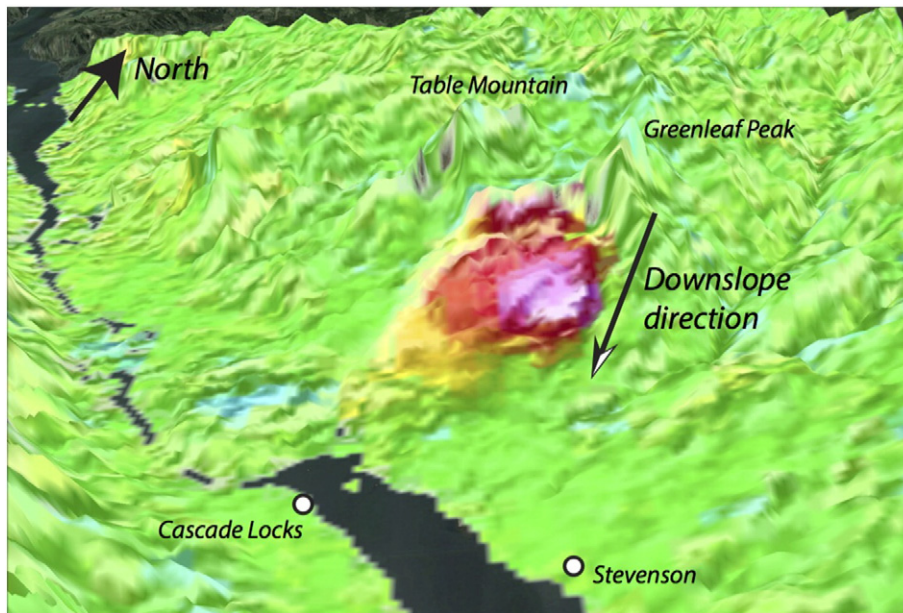


Fig. 5. A 3D perspective of landslide movement showing downslope motion from Google Earth. The color image of the velocity of the slow movements is draped on top of the topography. The color scale used is the same as Fig. 1b.

Table Mountain, and Greenleaf Peak are marked in Fig. 5. An arrow denotes the main downslope direction. There is anomalously fast movement at the base of the cliff south to the Greenleaf Peak probably due to settling of the talus (Palmer, 1977). The Bonneville landslide shows localized deformation near the toe; however, we suspect that the signal is associated with the InSAR phase decorrelation on the small lakes that reside on the toe.

The area enclosed by the active region of the Redbluff landslide reaches approximately 10.3 km² in total. The ground distance from the head to the toe of the active slide is about 4.8 km, and the width of the widest sliding zone is about 2.1 km. The maximum total LOS displacement is approximately 250 mm from 2007–2011, and the average line-of-sight (LOS) velocity reaches approximately 6 cm/yr. Given the look geometry of the satellite and downslope direction of the landslide, positive LOS would correspond to movement away from the satellite, which is consistent with downslope movement. If we assume a downslope dip angle of 5° and azimuth of 125° clockwise from North, then 6 cm/yr of average LOS velocity translates to approximately 15 cm/yr of average downslope velocity (Fig. 5).

4.2. Temporal behavior and seasonal variations

There is strong evidence to show that the landslide movement does not follow a constant rate or a simple sinusoidal function. Rather, the landslide exhibits a more complex spatial-temporal pattern that includes episodic movement (Fig. 4). The Redbluff landslide also exhibits seasonal movement, although this movement is variable from year-to-year. There are two periods of accelerated movement in the early winter of 2009 (i.e. from 11/08/2008 to 2/8/2009) and the early winter of 2011 (i.e. from 2010/11/14 to 2011/2/14). In contrast, more subtle movement is observed in the early winter of 2008 and 2010.

To further visualize the Redbluff landslide's temporal behavior, we extracted a cumulative displacement time-series at the center of the transport zone. The time series shows that the landslide's movement follows an annual cycle that correlates strongly with the seasons (Fig. 6). The displacement from the radar line-of-sight is first converted to downslope motion. The location of this displacement time-series is marked by an open circle in Fig. 4a. We label the months in the time axis to inspect any correlation of the downslope motion with the

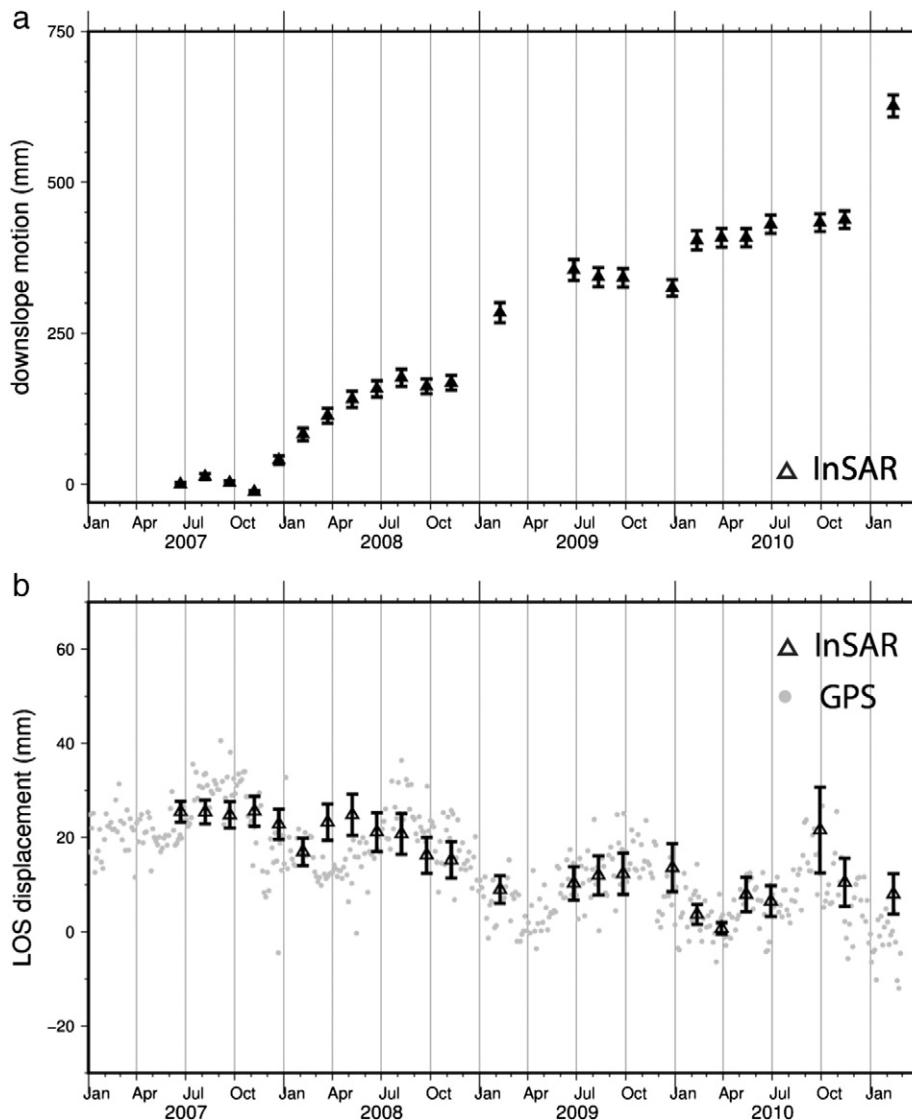


Fig. 6. (a) Cumulative downslope displacement in the deformation zone of the Redbluff landslide from the InSAR time-series analysis. The location of the deformation time series is marked in Fig. 4. (b) Comparison of the InSAR time-series with a nearby GPS station located adjacent to the landslide. Black triangles show the InSAR time-series at the location of the GPS site P429. Gray dots show the daily position measured by the GPS, and projected into the radar LOS direction for comparison. Negative LOS displacement corresponds to ground moving away from the satellite, i.e. subsidence. The error bars of the LOS displacement are estimated from the standard deviations of the InSAR data within a 1 km window surrounding the sample location.

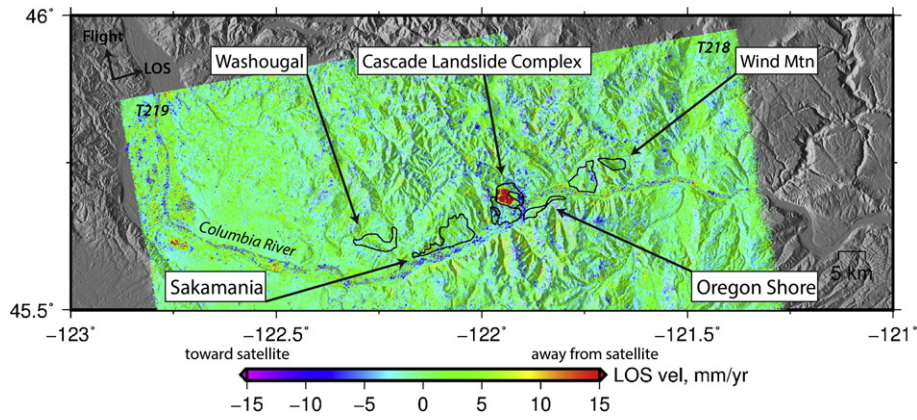


Fig. 7. An InSAR survey of active movement along the Columbia River Gorge, with a particular focus on previously mapped landslide deposits, including the Washougal, Sakamania, Cascade Landslide Complex, Oregon Shore, and Wind Mountain landslides. The line-of-site (LOS) velocity represents an average from 2007–2011. Note that the color scale saturates at 15 mm/yr.

seasons. The landslide activity is highest in the early winter (December, January, February), and lowest in the summer (June, July, August). We believe that the variable downslope motion from year-to-year is real, and not significantly biased by smoothing or the interferogram network used in the SBAS inversion. To support this, we also examine the subset of interferograms that span the 46-day period between each SAR acquisition. We display the consecutive chain of interferograms as an interferogram calendar, akin to a photo calendar, as shown in Fig. 3. The independent interferograms support two distinct periods of acceleration in early 2009 and 2011. The velocity peaks in the early winter season of each year, with the maximum LOS velocity of 60 cm/yr observed in the winter of 2011, in excellent agreement with the result shown in Fig. 4a.

4.3. Comparison with GPS data

While no continuous GPS stations are located on the active landslide, we compare our InSAR time series result using a nearby GPS

station located on the opposite bank of the Columbia River where no significant deformation is observed (Fig. 6b). We compared the InSAR displacement time-series with the GPS time-series from site P429 of the Plate Boundary Observatory. The GPS data are obtained from the UNAVCO data archive. In this comparison, the three component daily position time-series from GPS are projected into the LOS direction of the satellite. The tectonic motion in this region is removed from the GPS data before comparison with the InSAR data. The InSAR time-series is consistent with the independent GPS time-series, both of which exhibit an annual oscillation and a gradual trend of subsidence. The seasonal variations in the displacement time-series (Fig. 6b) are probably due to temperature variations, which change more regularly annually than the atmosphere water vapor (Dong et al., 2002). The uncertainties of the InSAR data are generally small, between 1–5 mm. While this comparison does not directly verify the movement of the landslide, it does give us some confidence that the SBAS result accurately measures the relative movements of the earth’s surface in our study area.

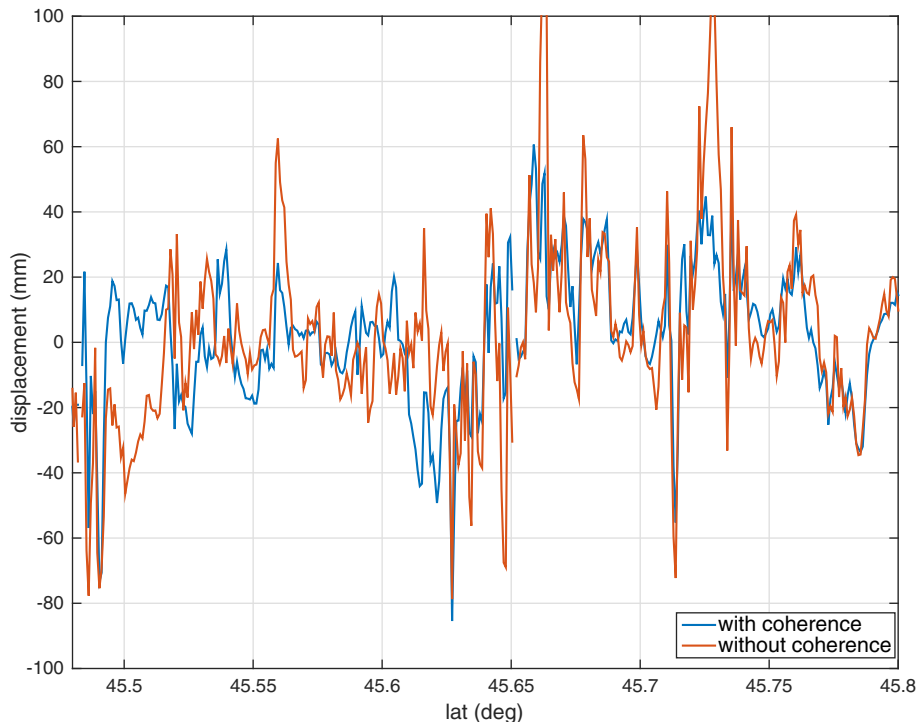


Fig. 8. Comparison of the LOS displacement profile from the InSAR time-series methods. The phase data are taken from Fig. 4a and b, epoch 11/08/2008.

4.4. Assessment of movement on nearby historical landslides

In addition to conducting an InSAR survey over the Cascade Landslide Complex, we extended our analysis to further downstream and upstream of the Columbia River where other large landslide complexes have been identified in past studies (Palmer, 1977; McCann and Forster, 1990). We processed the InSAR data along ALOS track 219, and overlaid the mapped boundaries of these known slides on top of the InSAR-derived velocity map (Fig. 7). We found no evidence of active movement at these mapped landslide complexes along the Columbia River Gorge, including the Washougal, Sakamania, and Oregon Shore landslides. While previous movement has been measured at the Wind Mountain landslide (Palmer, 1977), no contemporary movement is found during our observation period (2007 to 2011). Thus the Redbluff appears to be the only large landslide that is currently active along the Columbia River.

5. Discussion

5.1. Performance of the coherence-based SBAS method

Our analysis documents the spatial and temporal pattern of movement on the Redbluff landslide within the Cascade Landslide Complex. Despite the presence of dense vegetation, the L-band InSAR data provides excellent coherence. By incorporating a measure of decorrelation into our InSAR time series algorithm, we further bolster the spatial accuracy of our time series product. The coherent phase signal in the traditional SBAS time-series is limited to areas covered by bare ground or sparse vegetation, and the decorrelated pixels correspond to forested areas or lakes and ponds (Fig. 3). The dense vegetation causes temporal decorrelation in long time-span interferograms. With the coherence-weighting technique, we utilize all interferograms for each pixel, but downweight the decorrelated phase, to obtain a more complete picture of the deformation (Fig. 4).

We show the non-weighted SBAS result in comparison to the coherence-based result to illustrate the improvement from this modified processing method (Fig. 4b). The coherence-weighting algorithm retrieved a more robust pattern of deformation compared to the method with non-weighted SBAS. To be specific, the uniform weighting method resulted in some pixels exhibiting opposite sign to the downslope motion of the landslide. In Fig. 4a, the recovered signal is positive, corresponding to the downslope motion of the slide. But in Fig. 4b, we find several places of negative displacement lying to the north of the landslide boundary as well as at the toe of the Bonneville landslide. These differences are probably related to the noise caused by InSAR phase decorrelation. We show the comparison of the profiles of the cumulative displacements estimated from these two methods (Fig. 8). The profiles are extracted from one of the frames (i.e. on date 11/08/2009) in Fig. 4a and b and they run across the data grid from north to south at longitude -121.9° . The comparison illustrates that the coherence weighting scheme yield less variance in the displacement profile. The difference of these two profiles has a mean of 0.45 mm and a standard deviation of 19.8 mm. The Root Mean Square (RMS) reduction of the profiles is estimated to be 26.6%, which means that the new method can reduce the variance of the displacement values significantly without introducing much bias to the InSAR time-series. We conclude that the coherence-weighting method is able to yield a more coherent displacement map with fewer outliers and less phase variance.

5.2. Interpretation of movement on the Redbluff landslide

A comparison between the deformation pattern and the high-resolution topographic map from LiDAR reveals that the velocity field is correlated with the morphology of the landslide. There is a step change in the LOS velocity along the western boundary of the Redbluff landslide that maps along a ridge revealed by the LiDAR DEM. The up-slope

boundary of the Moseley Lake landslide is obscured. We hypothesize that the Redbluff landslide has overridden the former boundary of the Moseley Lake landslide (see arrow in Fig. 1). From the comparisons with the morphology revealed by the LiDAR data, we find that the region with the highest LOS velocity lies in the main body of the Redbluff landslide, which is between the headscarp at the hilltop and the hummocky topography at the base of the landslide. This region may be subsiding behind the active toe of the Redbluff landslide. We also identify a high velocity area at the base of the western headscarp.

We took profiles of the cumulative displacement field through time to visualize the potential growth pattern of the Redbluff landslide (Fig. 9). The profile is approximately 6 km long extending in northwest-southeast direction from the head to the toe of the Redbluff landslide. This profile is denoted by a dash line in Fig. 4a. Along this profile the elevation changes from 500 m at the head to 100 m at the toe. We find that the active movement concentrates at the main body of the slide. The active zone of the landslide corresponds to a hill slope with an elevation change of 300 m within 4 km horizontal distance. The active movement of the landslide is variable through the period of observation such that the cumulative motion doesn't simply scale through time. The downslope movement initiated at the upper slope region of the main body of the slide between 2008 and 2009. From 2009–2011, the downslope motion concentrates on two separate localities: one near the headscarp region and the other in the middle part of the landslide body. After 2011, there is a clear acceleration of the active movement in the middle part of the slide. We find that the upslope boundaries of the active slide are fixed through time, allowing us to map the active perimeter. However, the profiles after the fall of 2009 suggest that the downslope edges of the Redbluff landslide extended toward the toe region (Fig. 9).

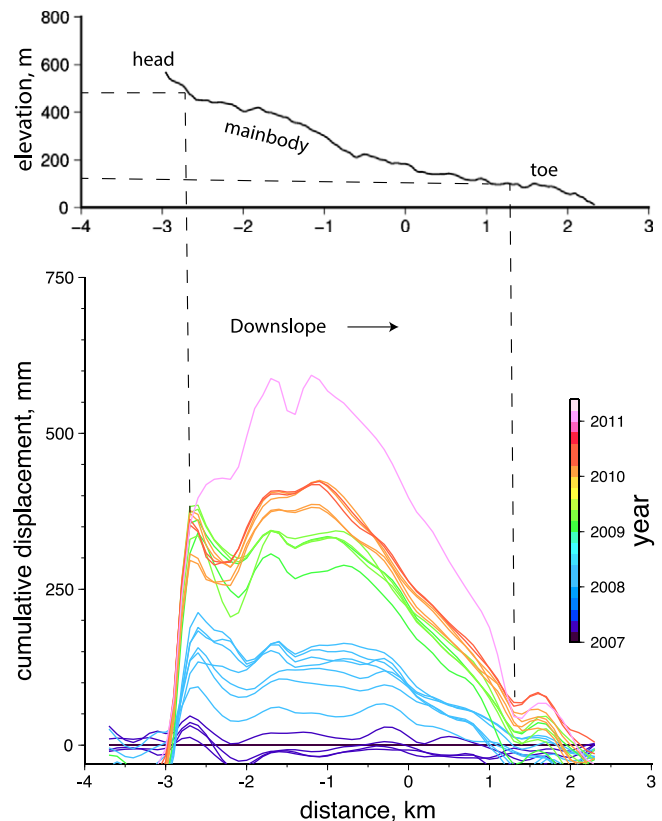


Fig. 9. Profile of the cumulative down-slope displacement time-series along the slope direction of the landslide. The headscarp of the slide is at -3 km and the toe of the slide is at 2 km. The sliding region is in the middle.

5.3. Correlation of rainfall and landslide movement

It is well documented that landslide activity is highly correlated to precipitation rates (De Vita and Reichenbach, 1998; Van Asch et al., 1999). Surface water ultimately infiltrates through the subsurface and raises pore pressure on the failure plane, which in turn reduces the effective normal stress and frictional resistance (Iverson and Major, 1987). To explore the relationship between landslide motion and precipitation for the Redbluff landslide, we compared the daily precipitation from a meteorological site near the Bonneville Dam with the

displacement time-series derived from InSAR (Fig. 10). To account for the coarser temporal sampling of the InSAR time series, we calculated the amount of precipitation during the same time periods of the InSAR observations using daily precipitation measurements, and compared this extracted precipitation time-series with the incremental displacement for each epoch derived from InSAR (Fig. 10b). This extra processing step allows us to better compensate for temporal sampling. In the Cascade Mountain Range, the wet season spans from October to May, while the summer and early fall remains dry. There are considerable variations in precipitation from one year to the next, representing the

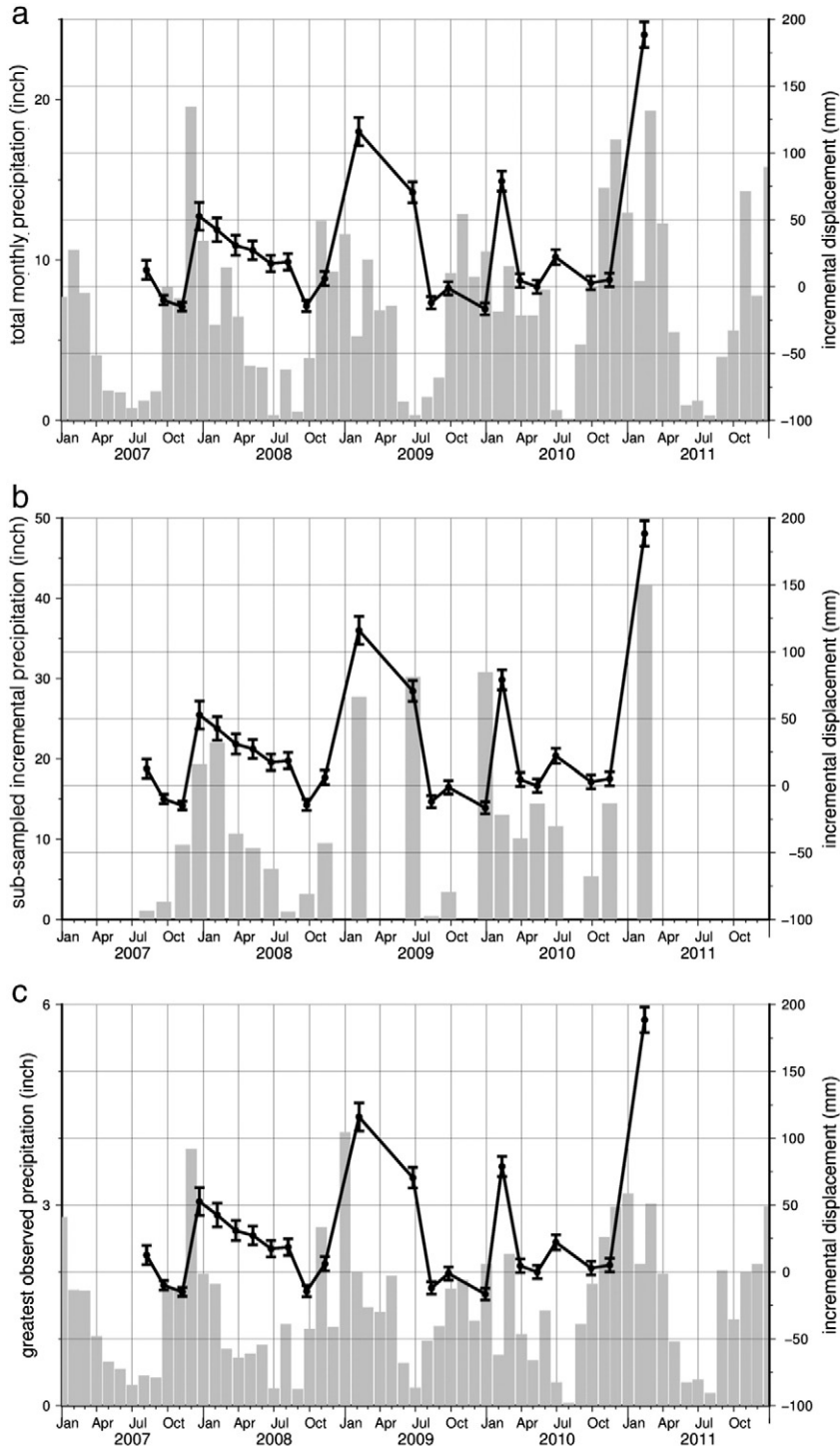


Fig. 10. Comparison of the incremental downslope displacement time-series (black lines) and the multiple precipitation data (gray histograms). (a) Monthly total precipitation. (b) Total precipitation extracted from the daily precipitation to sample the same temporal interval as the InSAR time-series. (c) Maximum daily precipitation observed each month.

short-term variability in climate forcing. We found a high correlation between the landslide movement and precipitation, which suggest that the activity of the landslide is governed by the external forcing from precipitation. Additionally we found that the first episode of accelerated movement on the CLC correlates with intensified rainfall in the winter season of 2008–2009. The second acceleration episode in winter 2010–2011 also correlates with a period of increased precipitation.

We also examined the variability of the maximum daily precipitation within each month to investigate the intensity and frequency of rainfall events (Fig. 10c). The maximum daily precipitation represents the greatest daily rainfall total within the time window of a month. A large maximum daily precipitation can be a proxy for intense rainfall events. A visual inspection suggests the accumulated rainfall is more strongly correlated with the landslide response than extreme rainfall events. This comparison reinforces the idea that the CLC is hydrologically driven and the activity is highly influenced by climatic forcing.

We present the correlation between the precipitation and the displacement to further probe the causality relationship between the landslide deformation and the rainfall (Fig. 11). We found that these data clearly exhibit a trend, consistent with previous studies that show how landslide failure is associated with the rainfall rate and duration (Schulz et al., 2009). It is evident that the increase in the sliding displacement is associated with the increase in the amount of rainfall, because there is a positive correlation between the displacement and the precipitation sampled at the same time period (Figs. 10b and 11). The correlation between precipitation and landslide motion can be understood using a hydraulic diffusion model that incorporates the hydraulic diffusivity and landslide depth (Iverson, 2000). Water from precipitation infiltrates into the basal shear zone by diffusion and reduces the effective normal stress of the slide. This kind of hydraulic forcing is particularly important for landslides on slopes covered by the loosely consolidated sediments.

We compared the kinematics of the Redbluff landslide to the geomorphological investigations of other landslides worldwide to shed light on the landslide dynamics in response to rainfall, groundwater level and atmospheric forcing. Through field evidence, Schulz et al. (2009) demonstrated that pore-water pressure increases following rainfall events caused reduced resistance to shear displacement. Malet et al. (2002) applied the GPS data on the Super-Sauze earthflow in France to determine a pore water pressure threshold that initiates accelerated movements. Our study further corroborates a conceptual model

of the landslide dynamics in which rainfall-modulated changes in pore pressure controls landslide movement. The detailed observations provided by field-based studies (Malet et al., 2002; Schulz et al., 2009) and the remote sensing data provided by this study could be integrated in the investigation of slow-moving landslides to help constrain the physical and hydrological parameters of the subsurface material (Baum et al., 2010; Handwerger et al., 2015; Iverson et al., 2015).

6. Conclusions

The Cascade Landslide Complex is one of many large landslide complexes along the Columbia River Gorge (Palmer, 1977). The continued monitoring of this system is critical for assessing the landslide hazard, particularly if the Redbluff, or other landslides, show evidence of anomalous behavior. The Columbia River Gorge is a critical transportation corridor, and a catastrophic landslide has the potential to overrun infrastructure and dam the river, which in turn raises the potential for downstream flooding. Our study provides a baseline assessment of active seasonal movement on the Redbluff. Similar to other active slow-moving landslides, the Redbluff landslide exhibits seasonal activity that is closely correlated with precipitation. Extreme precipitation events may raise the potential for accelerated movement in the future.

Acknowledgements

We thank Alaska Satellite Facility and JAXA for providing the ALOS-1 data. The Washington Department of Natural Resources and the Puget Sound Lidar Consortium provided the LiDAR data. We also thank UNACVO for providing the GPS time-series. Precipitation data are retrieved from NOAA's National Climatic Data Center. Funding is provided by NASA's Geodetic Imaging Program (Grant NNX13AC15G). We thank Tom Pierson, Susan Cashman, Alison Duvall, Benedikt Bayer and Harvey Greenburg for their help and discussions. The figures in the manuscript are made with Generic Mapping Tool (GMT) (Wessel et al., 2013).

References

- Agram, P.S., Simons, M., 2015. A noise model for InSAR time series. *J. Geophys. Res. Solid Earth* 120. <http://dx.doi.org/10.1002/2014JB01271>.
- Baum, R.L., Godt, J.W., Savage, W.Z., 2010. Estimating the timing and location of shallow rainfall-induced landslides using a model for transient, unsaturated infiltration. *J. Geophys. Res.* 115, F03013. <http://dx.doi.org/10.1029/2009JF001321>.
- Berardino, F., Fornaro, G., Lanari, R., Sansosti, E., 2002. A new algorithm for surface deformation monitoring based on small baseline differential SAR interferometry. *IEEE Trans. Geosci. Remote Sens.* 40, 2375–2383.
- Calabro, M.D., Schmidt, D.A., Roering, J.J., 2010. An examination of seasonal deformation at the Portuguese Bend landslide, southern California, using radar interferometry. *J. Geophys. Res.* 115, F02020. <http://dx.doi.org/10.1029/2009JF001314>.
- Chen, C.W., Zebker, H.A., 2000. Network approaches to two-dimensional phase unwrapping: intractability and two new algorithms. *JOSA A* 17 (3), 401–414. <http://dx.doi.org/10.1364/OSAA.17.000401>.
- Colesanti, C., Wasowski, J., 2006. Investigating landslides with space-borne Synthetic Aperture Radar (SAR) interferometry. *Eng. Geol.* 88 (3–4), 173–199. <http://dx.doi.org/10.1016/j.enggeo.2006.09.013> (ISSN 0013-7952).
- De Vita, P., Reichenbach, P., 1998. Rainfall-triggered landslides: a reference list. *Environ. Geol.* 35 (2–3), 219–233.
- Dong, D., Fang, P., Bock, Y., Cheng, M.K., Miyazaki, S., 2002. Anatomy of apparent seasonal variations from GPS-derived site position time series. *J. Geophys. Res.* 107 (B4). <http://dx.doi.org/10.1029/2001JB000573>.
- Farr, T.G., Kobrick, M., 2000. Shuttle radar topography mission produces a wealth of data. *EOS, Trans. Am. Geophys. Union* 81 (48), 583–585.
- Fattahi, H., Amelung, F., 2013. DEM error correction in InSAR time series. *IEEE Trans. Geosci. Remote Sens.* 51 (7), 4249–4259. <http://dx.doi.org/10.1109/TGRS.2012.2227761>.
- Ferretti, A., Prati, C., Rocca, F., 2001. Permanent scatterers in SAR interferometry. *IEEE Trans. Geosci. Remote Sens.* 39 (1), 8–20.
- Handwerger, A.L., Roering, J.J., Schmidt, D.A., 2013. Controls on the seasonal deformation of slow-moving landslides. *Earth Planet. Sci. Lett.* 377, 239–247.
- Handwerger, A.L., Roering, J.J., Schmidt, D.A., Rempel, A.W., 2015. Kinematics of earthflows in the northern California coast ranges using satellite interferometry. *Geomorphology* 246, 321–333. <http://dx.doi.org/10.1016/j.geomorph.2015.06.003> (ISSN 0169-555X).
- Hilley, G.E., Bürgmann, R., Ferretti, A., Novali, F., Rocca, F., 2004. Dynamics of slow-moving landslides from permanent scatterer analysis. *Science* 304, 1952–1955. <http://dx.doi.org/10.1126/science.1098821>.

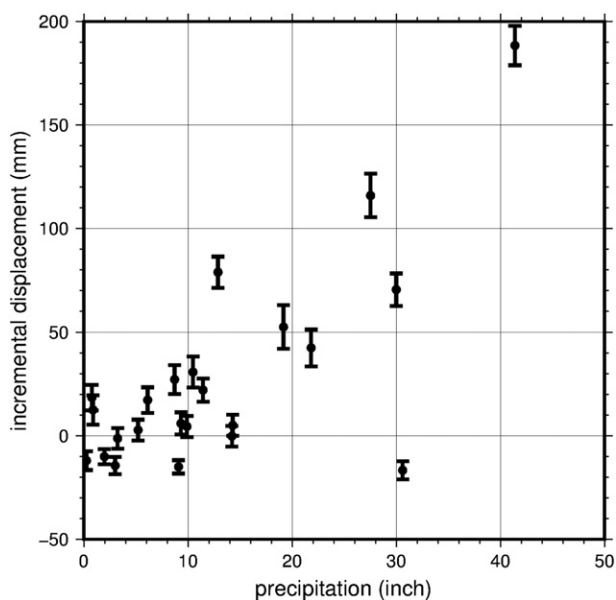


Fig. 11. Correlation between the precipitation and incremental displacement per InSAR epoch, see Fig. 10b.

- Iverson, R.M., 2000. Landslide triggering by rain infiltration. *Water Resour. Res.* 36, 1897–1910.
- Iverson, R.M., Major, J.J., 1987. Rainfall, groundwater flow, and seasonal movement at Minor Creek landslide, northwestern California: physical interpretation of empirical relations. *Geol. Soc. Am. Bull.* 99, 579–594.
- Iverson, R.M., George, D.L., Allstadt, K., Reid, M.E., Collins, B.D., Vallance, J.W., Schilling, S.P., Godt, J.W., Cannon, C.M., Magirl, C.S., Baum, R.L., 2015. Landslide mobility and hazards: implications of the 2014 Oso disaster. *Earth Planet. Sci. Lett.* 412, 197–208. <http://dx.doi.org/10.1016/j.epsl.2014.12.020>.
- Lanari, R., Mora, O., Mununta, M., Mallorqui, J., Berardino, P., Sansosti, E., 2004. A small baseline approach for investigating deformation on full resolution differential SAR interferograms. *IEEE Trans. Geosci. Remote Sens.* 42, 1377–1386.
- Lauknes, T.R., Zebker, H.A., Larsen, Y., 2011. InSAR deformation time series using an L1-norm small-baseline approach. *IEEE Trans. Geosci. Remote Sens.* 49 (1), 536–546.
- Malet, J.P., Van Asch, T.W., Van Beek, L.H., Maquaire, O., 2002. Distributed hydrological modelling of the Super-Sauze earthflow (south east France): implementation of the Starwars model. *Geomorphology, From Expert Opinion to Modelling*, pp. 65–72.
- McCann, D.M., Forster, A., 1990. Reconnaissance geophysical methods in landslide investigations. *Eng. Geol.* 29 (1), 59–78.
- Milillo, P., Fielding, E.J., Schulz, W.H., Delbridge, B., Bürgmann, R., 2014. COSMO-SkyMed spotlight interferometry over rural areas: the Slumgullion landslide in Colorado, USA. *IEEE J. Sel. Top. Appl. Earth Obs. Remote Sens.* 7 (7), 2919–2926. <http://dx.doi.org/10.1109/JSTARS.2014.2345664>.
- O'Connor, J.E., Burns, S.F., 2009. Cataclysms and controversy – aspects of the geomorphology of the Columbia River Gorge. *Geol. Soc. Am., Field Guid.* 15, 237–251. [http://dx.doi.org/10.1130/2009.fld015\(12\)](http://dx.doi.org/10.1130/2009.fld015(12)).
- O'Connor, J.E., Pierson, T.C., Turner, D., Atwater, B.F., Pringle, P.T., 1996. An exceptionally large Columbia River flood between 500 and 600 years ago – breaching of the Bridge-of-the-Gods landslide? *Geol. Soc. Am.* 28 (5), 97.
- Palmer, L., 1977. Large landslides of the Columbia River Gorge, Oregon and Washington. In: Coates, D.R. (Ed.), *Landslides: Geological Society of America. Reviews in Engineering Geology Vol. 3*, pp. 69–84.
- Pierson, T.C., Lu, Z., 2009. InSAR Detection of Renewed Movement of a Large Ancient Landslide in the Columbia River Gorge, Washington, Geological Society of America Abstract with Programs. Portland Annual Meeting. Vol. 41, p. 497 No. 7 http://gsa.confex.com/gsa/2009AM/finalprogram/abstract_162891.htm.
- Randall, J.R., 2012. Characterization of the Red Bluff Landslide, Greater Cascade Landslide Complex, Columbia River Gorge, Washington. *Dissertations and Theses. Paper 898* http://pdxscholar.library.pdx.edu/open_access_etds/898.
- Rosen, P.A., Hensley, S., Joughin, I.R., Li, F.K., Madsen, S.N., Rodriguez, E., Goldstein, R.M., 2000. Synthetic aperture radar interferometry. *Proc. IEEE* 88 (3).
- Sandwell, D.T., Mellors, R., Tong, X., Wei, M., Wessel, P., 2011. Open radar interferometry software for mapping surface deformation. *Eos Trans. AGU* 92 (28). <http://dx.doi.org/10.1029/2011EO280002>.
- Scheingross, J.S., Minchew, B.M., Mackey, B.H., Simons, M., Lamb, M.P., Hensley, S., 2013. Fault-zone controls on the spatial distribution of slow-moving landslides. *Geol. Soc. Am. Bull.* 125 (3–4), 473–489.
- Schmidt, D.A., Bürgmann, R., 2003. Time-dependent land uplift and subsidence in the Santa Clara valley, California, from a large interferometric synthetic aperture radar data set. *J. Geophys. Res.* 108 (B9), 2416. <http://dx.doi.org/10.1029/2002JB002267>.
- Schulz, W.H., McKenna, J.P., Kibler, J.D., Biavati, G., 2009. Relations between hydrology and velocity of a continuously moving landslide—evidence of pore-pressure feedback regulating landslide motion? *Landslides* 6, 181–190. <http://dx.doi.org/10.1007/s10346-009-0157-4>.
- Tong, X., Sandwell, D.T., Smith-Konter, B., 2013. High resolution interseismic velocity data along the San Andreas fault from GPS and InSAR. *J. Geophys. Res.* 118. <http://dx.doi.org/10.1029/2012JB009442>.
- Van Asch, T.W.J., Buma, J., Van Beek, L.P.H., 1999. A view on some hydrological triggering systems in landslides. *Geomorphology* 30 (1–2), 25–32. [http://dx.doi.org/10.1016/S0169-555X\(99\)00042-2](http://dx.doi.org/10.1016/S0169-555X(99)00042-2).
- Wasowski, J., Bovenga, F., 2014. Investigating landslides and unstable slopes with satellite multi temporal interferometry: current issues and future perspectives. *Eng. Geol.* 174, 103–138.
- Wessel, P., Smith, W.H.F., Scharroo, R., Luis, J.F., Wobbe, F., 2013. Generic mapping tools: improved version released. *EOS Trans. AGU* 94, 409–410.
- Wise, W.S., 1970. Cenozoic volcanism in the Cascade mountains of southern Washington. *Wash. State Dept. Nat. Resour. Bull.* 60, 1–44.
- Zhao, C.Y., Lu, Z., Zhang, Q., de la Fuente, J., 2012. Large area landslide detection and monitoring with ALOS/PALSAR imagery data over northern California and southern Oregon, USA. *Remote Sens. Environ.* 124, 348–359.